

Thermoelasticity and ArUco marker-based model validation of polymer structure: application to the San Giorgio's bridge inspection robot

Lorenzo Capponi¹, Tommaso Tocci¹, Mariapaola D'Imperio², Syed Haider Jawad Abidi², Massimiliano Scaccia², Ferdinando Cannella², Roberto Marsili¹, Gianluca Rossi¹

¹ Department of Engineering, University of Perugia, via G. Duranti 93, 06125 Perugia, Italy

² Industrial Robotic Unit, Istituto Italiano di Tecnologia, via Morego 30, 16163 Genova, Italy

ABSTRACT

Experimental procedures are often involved in the numerical models validation. To define the behaviour of a structure, its underlying dynamics and stress distributions are generally investigated. In this research, a multi-instrumental and multi-spectral method is proposed in order to validate the numerical model of the Inspection Robot mounted on the new San Giorgio's Bridge on the Polcevera river. An infrared thermoelasticity-based approach is used to measure stress-concentration factors and, additionally, an innovative methodology is implemented to define the natural frequencies of the Robot Inspection structure, based on the detection of ArUco fiducial markers. Established impact hammer procedure is also performed for the validation of the results.

Section: RESEARCH PAPER

Keywords: Thermoelasticity; ArUco markers; structural dynamics; carbon fibre reinforced polymer; robot inspection

Citation: Lorenzo Capponi, Tommaso Tocci, Mariapaola D'Imperio, Syed Haider Jawad Abidi, Massimiliano Scaccia, Ferdinando Cannella, Roberto Marsili, Gianluca Rossi, Thermoelasticity and ArUco marker-based model validation of polymer structure: application to the San Giorgio's bridge inspection robot, Acta IMEKO, vol. 10, no. 4, article 28, December 2021, identifier: IMEKO-ACTA-10 (2021)-04-28

Section Editor: Roberto Montanini, Università di Messina and Alfredo Cigada, Politecnico di Milano, Italy

Received July 30, 2021; **In final form** December 9, 2021; **Published** December 2021

Copyright: This is an open-access article distributed under the terms of the Creative Commons Attribution 3.0 License, which permits unrestricted use, distribution, and reproduction in any medium, provided the original author and source are credited.

Corresponding author: Lorenzo Capponi, e-mail: lorenzocapponi@outlook.it

1. INTRODUCTION

In design and materials engineering, experimental validation of numerical models is commonly required in order to verify the quality of the simulation [1], [2]. In general, the level of validation is directly tied to the intended use of the model and then, the supporting testing experiments are defined [3], [4]. While indirect validation uses experimental results that cannot be controlled by the user (e.g., from the literature or from previous researches), a direct approach performs experiments on the quantities of interest [5], with the aim of reproduce, through the experiments, actual behaviour of simulated model [4], [6].

When irregularities in the geometry or in the molecular-structure of the material are present, localised stress concentrations can lead to fractures [3]. Due to this, a stress concentration factor is usually considered during the design of a structure and, moreover, it is one of the experimental validations focuses. Local stress and strain measurements have been widely performed by means of established contact techniques (e.g.,

strain-gauges) [7]–[10]. However, in last decades, non-contact measurement methods for full-field stress and strain distribution estimation were developed and commonly employed in experimental validation tests, such as the Thermoelastic Stress Analysis (TSA) [11]. According to the thermoelastic effect, for a dynamically excited structure, the surface temperature changes, measured by means of an infrared detector, are proportional to the stress and strain tensors changes, caused by the input load [12]. Thermoelastic Stress Analysis was involved in multiple researches, regarding non-destructive testing [13], defect identification [14], and material properties characterization [15], [16]. Thermoelasticity has also been used to determine fatigue limit parameters and crack propagation [17], [18], for modal-damage identification in frequency domain [19], and for stress intensity factor evaluation in complex structures [20]. However, due to the demands of high-speed operation and the use of light structures in modern machinery, static measurements of stress and strain distributions are no longer sufficient [21], [22]. In fact, when a flexible structure is excited at or close to one of its natural frequencies, significantly increased fatigue damage occurs [23]–

[25]. Due to this, modal parameters (i.e., modal frequencies, modal damping and mode shapes) of structures and systems in frequency range of interest are widely researched to properly simulate their behaviour in real operating conditions [26], [27], and, thus, to avoid fatigue damage. Modal parameters definition is usually reached experimentally via impact-hammer procedure [26]. Nevertheless, in last years, the use of non-contact image-based measurement techniques in structural dynamics applications has grown. In fact, displacements, deformations and mode shapes can be measured with cameras operating in the visible spectrum by applying both Digital Image Correlation and other computer-vision methods [28]–[30]. One of the more promising approach for displacement and motion detection involves markers, either they are physical or virtual. Virtual markers are directly generated through computer-vision algorithms, such as Scale Invariant Feature Transform (SIFT) [31], [32], and Speeded Up Robust Features (SURF) [33]. These algorithms are able to detect and describe local characteristics (i.e., features) in images. Moreover, virtual markers are often used as they allow tracking objects in subsequent acquired frames without introducing physical targets, avoiding potential misleading elements. In recent years, several researches were developed using virtual markers. Khuc et al. [34] and Dong et al. [35] investigated structural and modal analysis via computer-vision algorithms through virtual markers. However, in the cases when the points of interest are not directly identified as markers, the physical targets need to be involved. Furthermore, virtual markers are strongly influenced by lighting changes and low contrast and, moreover, they can not be detected in uniform intensity distribution areas with no gradients. Physical markers, also known as fiducial markers, have been also widely employed in structural monitoring applications [36], [37]. A commonly employed group of fiducial markers are the Squared Planar Markers [38], which are characterized by a binary-coded squared area, enclosed by a black border. Several sets of this marker type have been developed in years [39]–[42]. However, in case of non-uniform light conditions and desired simultaneous detection of multiple markers, the ArUco marker library was found to be very efficacious and robust to detection errors and occlusion [38], [43]. Additionally, if the camera is calibrated, the relative position of the camera with respect to the markers can be directly estimated, and, through a custom configuration process, the system becomes more insensitive to detection errors and false positives [38]. Due to this, the ArUco markers applicability was widely studied in last years. Sani et al. [44] and Lebedev et al. [45] employed them for drone quad-rotor and UAV autonomous navigation and landing, while Elangovan et al. [46] used them for decoding contact forces exerted by adaptive hands. Structural dynamics applications were also researched by Abdelbarr et al.



Figure 1. Robot installed on the new Viaduct on the Polcevera river.

[47] for structural 3D displacement measurement. Moreover, Tocci et al. investigated the measurement uncertainty of the ArUco marker-based technique for displacement up to order of 1/100 mm, using a comparison Laser Doppler Vibrometry technique, defining the influence of the measurement parameters on the resulting measured displacement [48].

In this research, a non-contact multi-instrumental approach is presented for the numerical model results validation, which involves stress concentration factor evaluation through thermoelasticity measurements and natural frequencies identification by means of ArUco markers detection. The proposed method is applied to the San Giorgio's bridge Robot Inspection structure.

2. MATERIALS AND METHODS

2.1. Robot inspection

The Robot Inspection is the first platform for the automatic inspection of a bridge. It was developed within a collaboration between the Italian Institute of Technology, Camozzi Group, SDA Engineering, Ubisive and the University of Ancona (Patent PT190478), for the new Viaduct on the Polcevera river, the so-called San Giorgio's Bridge, designed and built after the Morandi's Bridge collapse. The structure is a 3-degrees-of-freedom platform, and it is fully autonomous. Its main purpose is to carry 3 technological instrumented supports with high performances cameras, lasers, ultrasonic sensors, and anemometers that scan the lower surface of the bridge and collect more than 35000 pictures. These pictures are then processed by Pattern Analysis Algorithms and given to the operator information whether any changes that on the investigated surface occurs. The robot weights around 1.8 t and it is shown in the Figure 1.

2.2. Thermoelasticity-based stress-concentration factor estimation

Thermoelasticity is a full-field stress-distribution measurement technique based on the thermoelastic effect [11], [12]. According to this effect, in case of adiabatic process and linear, homogeneous, and isotropic material behaviour, a dynamically excited structure presents surface temperature-changes proportional to the changes in the stress and strain tensor traces, caused by the external load [19], [49]. Moreover, if the excitation is harmonic, the thermal fluctuation is expected to be at the same frequency of the input load, and its normalized amplitude variation is given by:

$$\frac{\Delta T}{T_0} = -K_m \Delta \sigma_{kk}, \quad (1)$$

where T_0 is the ambient temperature, $\Delta \sigma_{kk}$ is the first stress invariant variation and K_m is the thermoelastic coefficient, defined from [11]:

$$K_m = \frac{\alpha}{\rho C_\sigma}, \quad (2)$$

where α is the thermal expansion coefficient, ρ is the material density and C_σ is the specific heat at constant pressure (or stress) [12]. In general, the temperature variation caused by the thermoelastic effect is within the noise produced by the infrared detector [50]. Thus, thermal acquisitions are necessarily post processed in order to obtain readable results [51]. Although general frequency-domain approaches are well established nowadays [19], [52], in this research a classical lock-in analysis

was performed in order to single out the thermoelastic signal at a particular frequency (i.e., the load frequency) from the noisy signal acquired through the thermal camera [53], [54]. Being ω_L the input load frequency, the digital lock-in amplifier gives the temperature fluctuation at ω_L as magnitude ΔT_{ω_L} and phase θ_{ω_L} [55]:

$$\Delta T_{\omega_L} = \sqrt{I_x^2(\omega_L) + I_y^2(\omega_L)}, \quad (3)$$

$$\theta_{\omega_L} = \arctan\left(\frac{I_y(\omega_L)}{I_x(\omega_L)}\right), \quad (4)$$

where $I_x(\omega_L)$ and $I_y(\omega_L)$ are the phasorial components of the thermoelastic signal evaluated at ω_L , respectively. Once applied the lock-in data processing, the spatial information of the temperature (i.e., stress) distribution is obtained, and further structural analysis can be performed. In particular, the stress-concentration factor K_f can be estimated in areas where critical behaviour is shown. K_f is defined, on a linear profile, as the ratio of the highest stress $\max(\Delta\sigma)$ and a reference stress, here chosen as the mean stress $\underline{\Delta\sigma}$ on the same profile [20]:

$$K_f = \frac{\max(\Delta\sigma)}{\underline{\Delta\sigma}}. \quad (5)$$

By substituting (1) in (5), the K_f factor on a linear profile becomes:

$$K_f = \frac{\max(\Delta T_{\omega_L})}{\underline{\Delta T_{\omega_L}}}. \quad (6)$$

2.3. ArUco-based resonant frequencies identification

As discussed earlier, the ArUco marker library was used for measurements, due to theoretical considerations [38]. An example of ArUco 6x6 marker is presented in Figure 2, which shows its geometrical parameters (i.e., corners and reference system).

To identify a marker in each captured frame, multiple steps are required [38], [43]. Firstly, a local-adaptive threshold contour segmentation is performed [56]. Then, a contour extraction and a polygonal approximation are applied to keep the enclosing rectangular borders and remove the irrelevant information [57]. Potential perspective projections are compensated using a

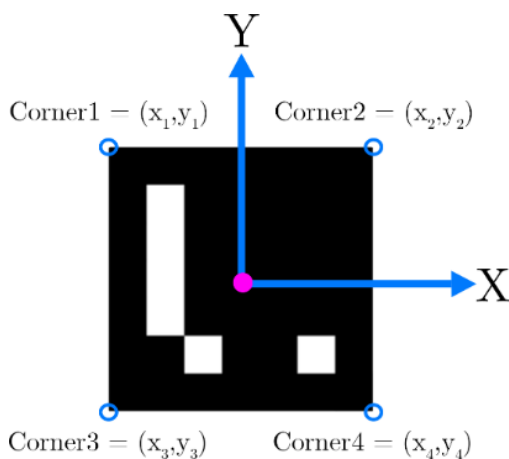


Figure 2. ArUco 6 × 6-marker: corners and centre coordinates.

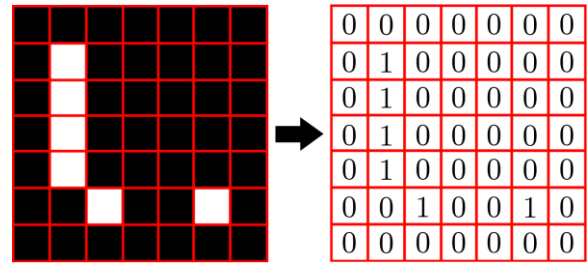


Figure 3. ArUco 6 × 6-marker: pixel values (example).

homography transformation. The resulting image is binarized and divided into a regular grid, where at each element is assigned 0 or 1, depending on the preponderant value of the corresponding pixel, as shown in Figure 3 [58].

ArUco markers are usually created in groups, to ensure their geometric diversity and avoid misleading detection. Due to this, another filter is generally applied to the image to determine potential matches between the recognized marker and the used marker-dictionary [43] even if manual corrections are normally made available by modifying threshold algorithm parameters. Finally, through the identification of the four corners, the spatial coordinates of each recognised marker are estimated with respect to the camera [38], [56]. In this study, the implementation of the ArUco library is exploited to measure the spatial temporal coordinates of the centre of the marker $\mathcal{C}(x(t), y(t))$ recorded in a video. Firstly, the acquired data are pre-processed to improve the marker detection, which, moreover, can be compromised by different factors (e.g., too much distance between the camera and the marker or blurred images measurement) [43]. Then, each frame is subjected to a sharpening and dilatation filters. The sharpening filter was used to reduce apparent blurring in each frame by means of 2D spatial convolution [59]:

$$(I * k)(x, y) = \sum_{i=-\infty}^{\infty} \sum_{j=-\infty}^{\infty} k(i, j) \cdot I(x - i, y - j) \quad (7)$$

where $I(x, y)$ is the original frame, $k(x, y)$ is the kernel and (x, y) are the pixel coordinates and (i, j) are the coordinates of the elements in the kernel matrix. Then, dilatation filter was also applied as a morphological operation, involved for removing noise, for isolating individual elements and for merging disparate elements in an image [59]. Also, this filter is based on convolution operation [60]. Being $b(x, y)$ the structuring function, by the grey-scale dilation of I by b is obtained [59]:

$$(I \oplus b)(x, y) = (i, j) \in \text{bmax} [I(x + i, y + j) + b(i, j)], \quad (8)$$

and the grey-scale erosion of I by b is given by:

$$(I \ominus b)(x, y) = (i, j) \in \text{bmin} [I(x + i, y + j) - b(i, j)]. \quad (9)$$

The marker detection is based on its 4 corners identification in each captured frame (see Figure 1). From the corners, the spatial coordinates of the centre of the marker (x_c, y_c) are evaluated frame-by-frame during the acquisition:

$$\mathcal{C} = (x_c, y_c) = G \cdot \left(\frac{1}{4} \sum_{r=1}^4 |x_r|, \frac{1}{4} \sum_{r=1}^4 |y_r| \right), \quad (10)$$

where (x_r, y_r) are the coordinates of the r -th vertex and G is the calibration factor from pixel units to SI units, defined as the ratio

between the side length of the physical marker in SI units and the average of the four side lengths (in pixels) of the captured marker in the FOV. Once the coordinates of the centre of the marker (x_c, y_c) in the time-domain are obtained, frequency domain-based analysis is performed using the Discrete Fourier Transform (DFT) [61]. The DFT for the N-points time series p is defined as:

$$P(\omega) = \sum_{n=0}^{N-1} p_n e^{-i\frac{n\omega}{N}}. \quad (11)$$

Considering the spatial properties of image-based analysis, the DFT for each component of the displacement $C(x_c(t), y_c(t))$ and for the input force $f(t)$ is obtained:

$$C(X(\omega), Y(\omega)) = (DFT(x(t)), DFT(y(t))), \quad (12)$$

$$F(\omega) = DFT(f(t)). \quad (13)$$

The cross-spectra (15) and auto-spectra (16) are computed [61]:

$$(S_{fx}(\omega), S_{fy}(\omega)) = \left(\frac{1}{T} [X(\omega)^* \cdot F(\omega)], \frac{1}{T} [Y(\omega)^* \cdot F(\omega)] \right), \quad (14)$$

$$S_{ff}(\omega) = \frac{1}{T} [F(\omega)^* \cdot F(\omega)]. \quad (15)$$

Finally, the compliance Frequency Response Functions (FRF) along x-axis and y-axis, using H_1 estimator, can be obtained [61]:

$$(H_{1x}(\omega), H_{1y}(\omega)) = \left(\frac{S_{fx}(\omega)}{S_{ff}(\omega)}, \frac{S_{fy}(\omega)}{S_{ff}(\omega)} \right). \quad (16)$$

On the other hand, the acceleration Frequency Response Function obtained through the impact hammer procedure is given using the H_1 estimator by [61]:

$$H_1 = \frac{S_{fa}(\omega)}{S_{ff}(\omega)}, \quad (17)$$

where S_{fa} and S_{ff} are the cross- and auto-spectra of the output acceleration and of the input force, respectively.

3. EXPERIMENTAL METHODOLOGY

As already addressed in Sec. 2, two different measurement approaches were used and, due to this, two experimental setups were built. The global tested structure is presented in Figure 4, where the analysed areas and markers are shown in detail: thermoelasticity was applied in T1 and T2 areas, while M1-2 is



Figure 4. Tested CFRP structure: T1) First TSA analysed area; T2) Second TSA analysed area; M1-2) ArUco marker detected.

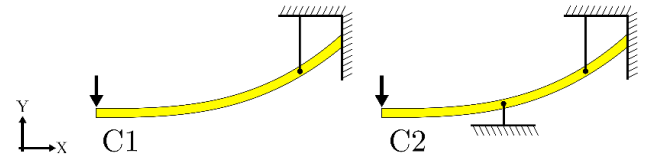


Figure 5. Boundary configurations of the structure: C1) single fixed constraint; C2) double fixed constraint..

the ID of the marker detected whose results are presented in this research. In fact, as shown in Figure 4, 13 markers have been mounted on the structure and multiple measurements, of single markers and of groups of them, were performed. For this reason, for the sake of clarity, only results related to the marker at the tip of the structure (i.e., M1-2) are presented.

Moreover, the structure was tested in two different boundary configurations, that are schematized in Figure 5.

In this manuscript, the authors will refer to the configuration with one fixed constraint as C1 configuration and as C2 configuration to the one with two fixed constraints. For the sake of clarity, the experiments are combined as follows: T1 area was analysed in C1 configuration, T2 area in C2 configuration and the M1-2 marker was detected in both C1 and C2 configurations.

3.1. Thermoelasticity

The Thermoelastic Stress Analysis was performed as explained in Sec. 2.2. Firstly, the yellow painting was removed, and a proper matt black wrapper paint was used for the surface conditioning, due to theoretical considerations [55]: the emissivity of the surface was increased and homogenized, and appreciable results were thus obtained. Then, a harmonic load at 1.1 Hz and 2.7 Hz were given to the structure in T1 and T2 analysed area, respectively, and the temperature changes of the surface were measured, in each test, for 60 seconds with a MWIR cooled thermal camera FLIR A6751sc, operating at 125 Hz of sampling rate and 640×512 pixels of resolution.

3.2. ArUco-based resonant frequencies identification

In order to define the natural frequencies of the tested structure, classic impact hammer procedure was also performed to validate further the results obtained through image-based analysis. Due to this, a PCB 086D20 hammer was used for the input broadband excitation, a uniaxial PCB 352C34 amplified accelerometer and a PicoScope data acquisition system. The accelerometer was positioned on the tip of the structure, along the y-axis of the system. Input and output data were acquired at 1 kHz for 50 seconds of duration. Simultaneously with the impact hammer tests, a Canon EOS 7D camera, mounting a 24-70 mm optic (F 2.8), was used for measuring the position of the framed markers. Spatial resolution of 1920×1080 pixels and sampling frequency of 30 Hz were used as acquisition parameters. In this experiment, a 6x6 bit ArUco marker dictionary was used.

4. RESULTS

4.1. Stress concentration factor

The stress concentration factor was evaluated in two critical areas, T1 and T2, whose thermal acquisitions and finite element models are shown in Figure 6 and Figure 7, respectively.

By means of (3), the lock-in analysis was performed and the magnitude of the thermoelastic signal is shown in Figure 8 and Figure 9, where it is compared to the data obtained from the

numerical simulation in the same corresponding linear region of interest.

The stress concentration factors K_f , as described by (6), were evaluated from the profiles in Figure 7 and Figure 8, and they are shown in Table 1, obtained from the experiments and the FEM model.

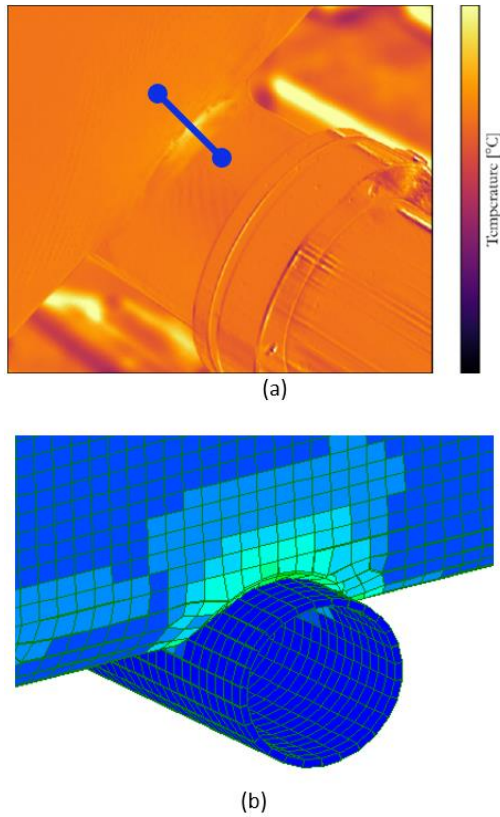


Figure 6. T1 area stress profile: (a) Experimental; (b) Numerical.

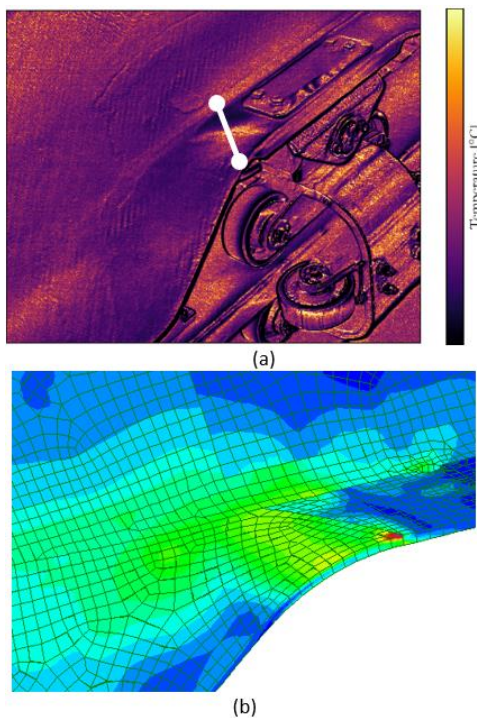


Figure 7. T2 area stress profile: (a) Experimental; (b) Numerical.

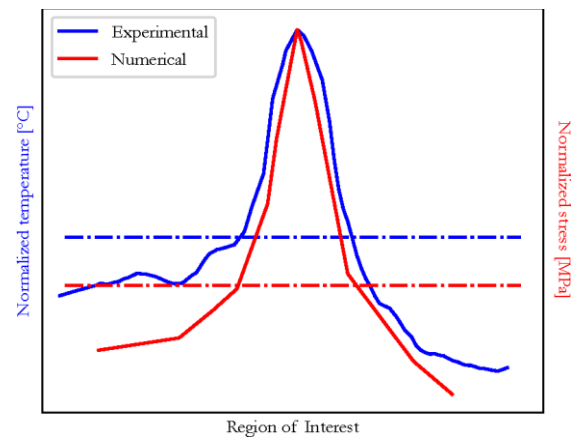


Figure 8. T1 area stress and temperature profiles.

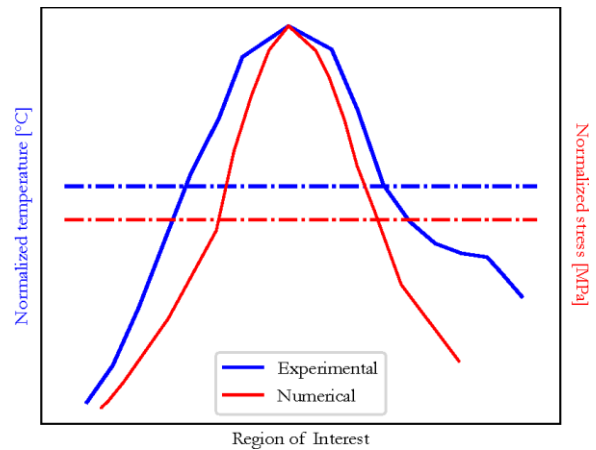


Figure 9. T2 area stress and temperature profiles.

The obtained results are in line with the expectations. In fact, usually, the thermoelasticity slightly underestimate the stress, due to theoretical considerations, but, principally, actual stresses measured on the structure are presumed to be lower than the numerical values due to designing consideration.

4.2. ArUco-based resonant frequencies identification

As already addressed in Sec. 3.3, firstly, the marker position in the time-domain was collected using modal testing procedure (see Figure 10) through (10), and then the FRF was obtained using (16). The Frequency Response Functions were reconstructed using the Least-Squares Complex Exponential (LSCE) algorithm [62].

The FRFs obtained by means of the two experimental methods are shown in Figure 11 and Figure 12 for C1 and C2 boundary configurations, respectively. Although in the amplitudes are different (the marker gave compliance FRF while the impact hammer gave acceleration FRF), the natural frequencies identified along the x-axis are totally comparable.

Furthermore, the comparison with the numerical simulation was performed and it is shown in Figure 13 and Figure 14, in terms of normalized frequency for C1 and C2 boundary configurations, respectively.

Table 1. Stress concentration factors results.

	T1 area	T2 area
Experiments	1.19	1.21
Numerical	2.40	1.40

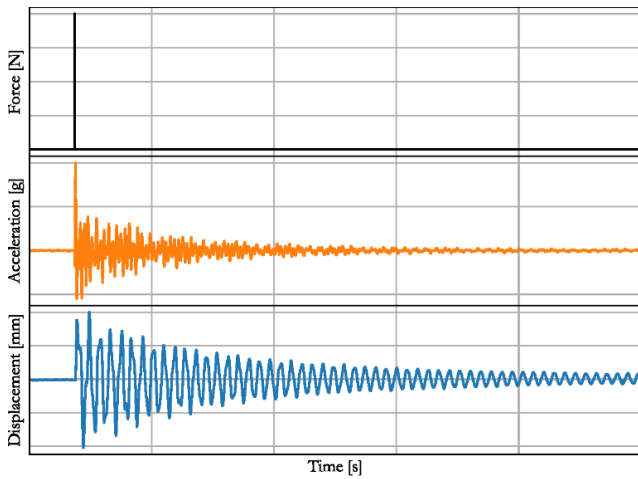


Figure 10. Modal testing procedure: input impulse and damped output signals from accelerometer and ArUco marker.

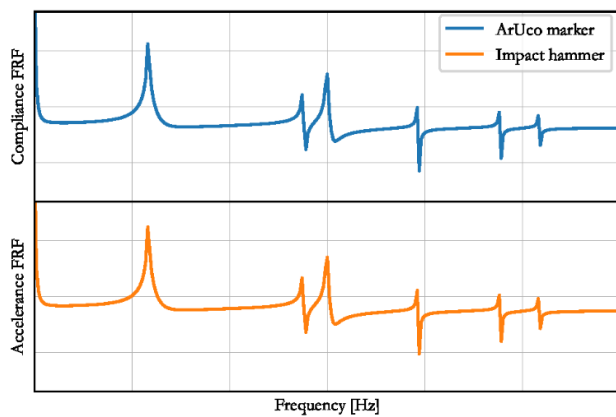


Figure 11. Frequency Response Function using ArUco markers and impact hammer: C1 boundary configuration.

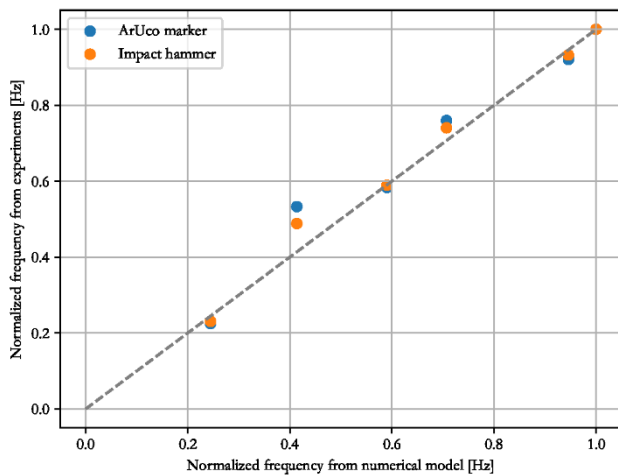


Figure 12. Frequency Response Function using ArUco markers and impact hammer: C2 boundary configuration.

The results show a well-founded numerical model. In fact, the comparison of the experimental resonant frequencies, obtained using impact hammer and ArUco markers, with the numerical results establish high reliability in both the two boundary condition configurations, for all the modes in the considered frequency range.

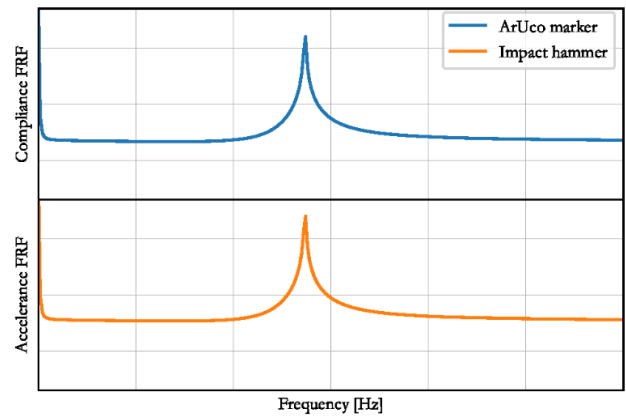


Figure 13. Frequency Response Function using ArUco markers and impact hammer: C2 boundary configuration.

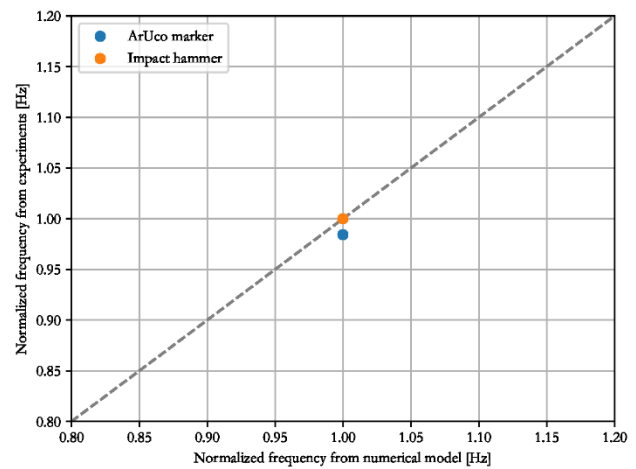


Figure 14. Natural frequencies comparison: C2 boundary configuration.

5. CONCLUSIONS

The validation of numerical models through experimental procedures is a mandatory step for several applications. In this research, a non-contact multi-instrumental approach was proposed to validate the numerical model of the Robot Inspection of the new San Giorgio's Bridge on the Polcevera river. In particular, the thermoelastic technique was used to measure stress-concentration factors in two areas and, moreover, an innovative methodology, involving the detection of the ArUco fiducial markers, was implemented to define the resonant frequencies of the CFRP structure, by estimating its Frequency Response Function. The impact-hammer procedure was also performed for the validation of the results. The proposed approach gave excellent results and, due to this, it can be used for testing large structures. Further investigations on the material properties and on the dynamics of the Inspection Robot are planned as extension of this research.

ACKNOWLEDGEMENT

The authors acknowledge Camozzi Group and SDA Engineering for allowing and supporting this research through the collaboration with the Italian Institute of Technology. Moreover, Ubisive, Fincantieri and PerGenova participated in this research with the University of Ancona (Univpm).

REFERENCES

- [1] X. D. Li, N. E. Wiberg, Structural dynamic analysis by a time-discontinuous Galerkin finite element method, *Int. J. Numer. Methods Eng.*, vol. 39, no. 12, 1996, pp. 2131–2152. DOI: [10.1002/\(SICI\)1097-0207\(19960630\)39:12%3C2131::AID-NME947%3E3.0.CO;2-Z](https://doi.org/10.1002/(SICI)1097-0207(19960630)39:12%3C2131::AID-NME947%3E3.0.CO;2-Z)
- [2] F. Cianetti, G. Morettini, M. Palmieri, G. Zucca, Virtual qualification of aircraft parts: Test simulation or acceptable evidence?, *Procedia Struct. Integr.*, vol. 24, no. 2019, 2019, pp. 526–540. DOI: [10.1016/j.prostr.2020.02.047](https://doi.org/10.1016/j.prostr.2020.02.047)
- [3] R. C. Juvinall, K. M. Marshek, *Fundamentals of machine component design*, vol. 83. John Wiley & Sons New York, 2006.
- [4] A. Lavatelli, E. Zappa, Uncertainty in vision based modal analysis: probabilistic studies and experimental validation, *Acta IMEKO*, vol. 5, no. 4, 2016, pp. 37-48. DOI: [10.21014/acta_imeko.v5i4.426](https://doi.org/10.21014/acta_imeko.v5i4.426)
- [5] A. C. Jones, R. K. Wilcox, Finite element analysis of the spine: towards a framework of verification, validation and sensitivity analysis, *Med. Eng. Phys.*, vol. 30, no. 10, 2008, pp. 1287–1304. DOI: [10.1016/j.medengphy.2008.09.006](https://doi.org/10.1016/j.medengphy.2008.09.006)
- [6] G. Morettini, C. Braccesi, F. Cianetti, Experimental multiaxial fatigue tests realized with newly developed geometry specimens, *Fatigue Fract. Eng. Mater. Struct.*, vol. 42, no. 4, 2019, pp. 827–837. DOI: [10.1111/ffe.12954](https://doi.org/10.1111/ffe.12954)
- [7] E. O. Doebelin, D. N. Manik, *Measurement systems: application and design*, McGraw-Hill College, 2007, ISBN 978-0072922011.
- [8] A. Schäfer, High-precision amplifiers for strain gauge based transducers—first time realized in compact size, *ACTA IMEKO*, vol. 6, no. 4, 2017, pp. 31-36. DOI: [10.21014/acta_imeko.v6i4.477](https://doi.org/10.21014/acta_imeko.v6i4.477)
- [9] Z. Lai, Y. Xiaoxiang, Y. Jinhui, Vibration analysis of the oscillation support of column load cells in low speed axle-group weigh-in-motion system, *ACTA IMEKO*, vol. 9, no. 5, pp 63-69, 2020. DOI: [10.21014/acta_imeko.v9i5.940](https://doi.org/10.21014/acta_imeko.v9i5.940)
- [10] L. Capponi, M. Česnik, J. Slavič, F. Cianetti, M. Boltežar, Non-stationarity index in vibration fatigue: Theoretical and experimental research, *Int. J. Fatigue*, vol. 104, 2017, pp. 221–230. DOI: [10.1016/j.ijfatigue.2017.07.020](https://doi.org/10.1016/j.ijfatigue.2017.07.020)
- [11] W. Thomson, On the Dynamical Theory of Heat, *Transactions of the Royal Society of Edinburgh*, vol. 20, no. 2, pp. 261-288, 1853. DOI: [10.1017/S0080456800033172](https://doi.org/10.1017/S0080456800033172)
- [12] W. Weber, Über die spezifische Wärme fester Körper, insbesondere der Metalle, *Ann. Phys.*, vol. 96, no. 10, pp. 177–213, 1830.
- [13] J. Qiu, C. Pei, H. Liu, and Z. Chen, Quantitative evaluation of surface crack depth with laser spot thermography, *Int. J. Fatigue*, vol. 101, pp. 80–85, 2017. DOI: [10.1016/j.ijfatigue.2017.02.027](https://doi.org/10.1016/j.ijfatigue.2017.02.027)
- [14] X. Guo and Y. Mao, Defect identification based on parameter estimation of histogram in ultrasonic IR thermography, *Mech. Syst. Signal Process.*, vol. 58, pp. 218–227, 2015. DOI: [10.1016/j.ymssp.2014.12.011](https://doi.org/10.1016/j.ymssp.2014.12.011)
- [15] G. Allevi, L. Capponi, P. Castellini, P. Chiariotti, F. Docchio, F. Freni, R. Marsili, M. Martarelli, R. Montanini, S. Pasinetti, A. Quattrocchi, R. Rossetti, G. Rossi, G. Sansoni, E. P. Tomasini, Investigating additive manufactured lattice structures: a multi-instrument approach, *IEEE Trans. Instrum. Meas.*, 2019. DOI: [10.1109/TIM.2019.2959293](https://doi.org/10.1109/TIM.2019.2959293)
- [16] F. Cannella, A. Garinei, M. D’Imperio, G. Rossi, A novel method for the design of prostheses based on thermoelastic stress analysis and finite element analysis, *J. Mech. Med. Biol.*, vol. 14, no. 05, p. 1450064, 2014. DOI: [10.1142/S021951941450064X](https://doi.org/10.1142/S021951941450064X)
- [17] G. Fargione, A. Geraci, G. La Rosa, A. Risitano, Rapid determination of the fatigue curve by the thermographic method, *Int. J. Fatigue*, vol. 24, no. 1, pp. 11–19, 2002. DOI: [10.1016/S0142-1123\(01\)00107-4](https://doi.org/10.1016/S0142-1123(01)00107-4)
- [18] X. D. Li, H. Zhang, D. L. Wu, X. Liu, J. Y. Liu, Adopting lock-in infrared thermography technique for rapid determination of fatigue limit of aluminum alloy riveted component and affection to determined result caused by initial stress, *Int. J. Fatigue*, vol. 36, no. 1, 2012, pp. 18–23. DOI: [10.1016/j.ijfatigue.2011.09.005](https://doi.org/10.1016/j.ijfatigue.2011.09.005)
- [19] L. Capponi, J. Slavič, G. Rossi, M. Boltežar, Thermoelasticity-based modal damage identification, *Int. J. Fatigue*, vol. 137, Aug. 2020, p. 105661. DOI: [10.1016/j.ijfatigue.2020.105661](https://doi.org/10.1016/j.ijfatigue.2020.105661)
- [20] R. Marsili and G. Rossi, TSA infrared measurements for stress distribution on car elements, *J. Sensors Sens. Syst.*, vol. 6, no. 2, p. 361, 2017. DOI: [10.5194/jsss-6-361-2017](https://doi.org/10.5194/jsss-6-361-2017)
- [21] M. D’Imperio, D. Ludovico, C. Pizzamiglio, C. Canali, D. Caldwell, F. Cannella, FLEGX: A bioinspired design for a jumping humanoid leg, in *2017 IEEE/RSJ International Conference on Intelligent Robots and Systems (IROS)*, 2017, pp. 3977–3982. DOI: [10.1109/IROS.2017.8206251](https://doi.org/10.1109/IROS.2017.8206251)
- [22] J. Schijve, *Fatigue of structures and materials*. Springer Science & Business Media, 2001, ISBN 978-1402068072
- [23] D. Benasciutti, F. Sherratt, and A. Cristofori, Basic Principles of Spectral Multi-axial Fatigue Analysis, *Procedia Eng.*, vol. 101, pp. 34–42, 2015. DOI: [10.1016/j.proeng.2015.02.006](https://doi.org/10.1016/j.proeng.2015.02.006)
- [24] P. Wolfsteiner, A. Trapp, Fatigue life due to non-Gaussian excitation—An analysis of the Fatigue Damage Spectrum using Higher Order Spectra, *Int. J. Fatigue*, vol. 127, pp. 203–216, 2019. DOI: [10.1016/j.ijfatigue.2019.06.005](https://doi.org/10.1016/j.ijfatigue.2019.06.005)
- [25] G. Morettini, C. Braccesi, F. Cianetti, S. M. J. Razavi, K. Solberg, L. Capponi, Collection of experimental data for multiaxial fatigue criteria verification, *Fatigue Fract. Eng. Mater. Struct.*, vol. 43, no. 1, pp. 162–174, 2020. DOI: [10.1111/ffe.13101](https://doi.org/10.1111/ffe.13101)
- [26] D. J. Ewins, *Modal testing: theory and practice*. Hertfordshire, UK, 1986, ISBN: 978-0863802188.
- [27] M. Mršnik, J. Slavič, M. Boltežar, Vibration fatigue using modal decomposition, *Mech. Syst. Signal Process.*, vol. 98, pp. 548–556, 2018. DOI: [10.1016/j.ymssp.2017.03.052](https://doi.org/10.1016/j.ymssp.2017.03.052)
- [28] B. D. Lucas, T. Kanade, An iterative image registration technique with an application to stereo vision, *Proc. DARPA Image Underst. Work.*, pp. 121–130, 1981.
- [29] J. Javh, J. Slavič, and M. Boltežar, Experimental modal analysis on full-field DSLR camera footage using spectral optical flow imaging, *J. Sound Vib.*, vol. 434, pp. 213–220, 2018. DOI: [10.1016/j.jsv.2018.07.046](https://doi.org/10.1016/j.jsv.2018.07.046)
- [30] D. Gorjup, J. Slavič, M. Boltežar, Frequency domain triangulation for full-field 3D operating-deflection-shape identification, *Mech. Syst. Signal Process.*, vol. 133, p. 106287, 2019. DOI: [10.1016/j.ymssp.2019.106287](https://doi.org/10.1016/j.ymssp.2019.106287)
- [31] T. Tocci, L. Capponi, R. Marsili, G. Rossi, J. Pirisinu, Suction system vapour velocity map estimation through SIFT-based algorithm, in *Journal of Physics: Conference Series*, 2020, vol. 1589, no. 1, p. 12004. DOI: [10.1088/1742-6596/1589/1/012004](https://doi.org/10.1088/1742-6596/1589/1/012004)
- [32] G. Allevi, L. Casacanditella, L. Capponi, R. Marsili, G. Rossi, Census Transform Based Optical Flow for Motion Detection during Different Sinusoidal Brightness Variations, *Journal of Physics: Conference Series*, 2018, vol. 1149, no. 1, p. 12032. DOI: [10.1088/1742-6596/1149/1/012032](https://doi.org/10.1088/1742-6596/1149/1/012032)
- [33] H. Bay, T. Tuytelaars, L. Van Gool, Surf: Speeded up robust features, *European conference on computer vision*, 2006, pp. 404–417. DOI: [10.1007/11744023_32](https://doi.org/10.1007/11744023_32)
- [34] T. Khuc, F. Catbas, Computer vision-based displacement and vibration monitoring without using physical target on structures, *Struct. Infrastruct. Eng.*, vol. 13, no. 4, pp. 505–516, 2017. DOI: [10.1080/15732479.2016.1164729](https://doi.org/10.1080/15732479.2016.1164729)

- [35] C. Dong, O. Celik, and F. Catbas, Marker-free monitoring of the grandstand structures and modal identification using computer vision methods, *Struct. Heal. Monit.*, vol. 18, no. 5–6, pp. 1491–1509, 2019.
DOI: [10.1177/1475921718806895](https://doi.org/10.1177/1475921718806895)
- [36] F. Lunghi, A. Pavese, S. Peloso, I. Lanese, D. Silvestri, Computer vision system for monitoring in dynamic structural testing, in *Role of seismic testing facilities in performance-based earthquake engineering*, Springer, pp. 159–176, 2012.
DOI: [10.1007/978-94-007-1977-4](https://doi.org/10.1007/978-94-007-1977-4)
- [37] S. W. Park, H. S. Park, J. H. Kim, H. Adeli, 3D displacement measurement model for health monitoring of structures using a motion capture system, *Measurement*, vol. 59, pp. 352–362, 2015.
DOI: [10.1016/j.measurement.2014.09.063](https://doi.org/10.1016/j.measurement.2014.09.063)
- [38] F. J. Romero-Ramirez, R. Muñoz-Salinas, and R. Medina-Carnicer, Speeded up detection of squared fiducial markers, *Image Vis. Comput.*, vol. 76, pp. 38–47, 2018.
DOI: [10.1016/j.imavis.2018.05.004](https://doi.org/10.1016/j.imavis.2018.05.004)
- [39] H. Kato, M. Billingham, Marker tracking and hmd calibration for a video-based augmented reality conferencing system, in *Proceedings 2nd IEEE and ACM International Workshop on Augmented Reality (IWAR'99)*, 1999, pp. 85–94.
DOI: [10.1109/IWAR.1999.803809](https://doi.org/10.1109/IWAR.1999.803809)
- [40] M. Fiala, Designing highly reliable fiducial markers, *IEEE Trans. Pattern Anal. Mach. Intell.*, vol. 32, no. 7, pp. 1317–1324, 2009.
DOI: [10.1109/TPAMI.2009.146](https://doi.org/10.1109/TPAMI.2009.146)
- [41] D. Flohr, J. Fischer, A lightweight ID-based extension for marker tracking systems, *The Eurographics Association*, 2007.
DOI: [10.2312/PE/VE2007Short/059-064](https://doi.org/10.2312/PE/VE2007Short/059-064)
- [42] E. Olson, AprilTag: A robust and flexible visual fiducial system, in *2011 IEEE International Conference on Robotics and Automation*, 2011, pp. 3400–3407.
DOI: [10.1109/ICRA.2011.5979561](https://doi.org/10.1109/ICRA.2011.5979561)
- [43] S. Garrido-Jurado, R. Muñoz-Salinas, F. J. Madrid-Cuevas, M. J. Marín-Jiménez, Automatic generation and detection of highly reliable fiducial markers under occlusion, *Pattern Recognit.*, vol. 47, no. 6, pp. 2280–2292, 2014.
DOI: [10.1016/j.patcog.2014.01.005](https://doi.org/10.1016/j.patcog.2014.01.005)
- [44] M. F. Sani, G. Karimian, Automatic navigation and landing of an indoor AR. drone quadrotor using ArUco marker and inertial sensors, *2017 International Conference on Computer and Drone Applications (IconDA)*, 2017, pp. 102–107.
DOI: [10.1109/ICONDA.2017.8270408](https://doi.org/10.1109/ICONDA.2017.8270408)
- [45] I. Lebedev, A. Erashov, A. Shabanova, Accurate Autonomous UAV Landing Using Vision-Based Detection of ArUco-Marker, *International Conference on Interactive Collaborative Robotics*, 2020, pp. 179–188.
DOI: [10.1007/978-3-030-60337-3_18](https://doi.org/10.1007/978-3-030-60337-3_18)
- [46] N. Elangovan, A. Dwivedi, L. Gerez, C. Chang, M. Liarokapis, Employing IMU and ArUco Marker Based Tracking to Decode the Contact Forces Exerted by Adaptive Hands, *2019 IEEE-RAS 19th International Conference on Humanoid Robots (Humanoids)*, 2019, pp. 525–530.
DOI: [10.1109/Humanoids43949.2019.9035051](https://doi.org/10.1109/Humanoids43949.2019.9035051)
- [47] M. Abdelbarr, Y. L. Chen, M. R. Jahanshahi, S. F. Masri, W. Shen, U. Qidwai, 3D dynamic displacement-field measurement for structural health monitoring using inexpensive RGB-D based sensor, *Smart Mater. Struct.*, vol. 26, no. 12, p. 125016, 2017.
DOI: [10.1088/1361-665X/aa9450](https://doi.org/10.1088/1361-665X/aa9450)
- [48] T. Tocci, L. Capponi, and G. Rossi, ArUco marker-based displacement measurement technique: uncertainty analysis, *Eng. Res. Express* (2021)
DOI: [10.1088/2631-8695/ac1fc7](https://doi.org/10.1088/2631-8695/ac1fc7)
- [49] W. N. Sharpe, *Springer handbook of experimental solid mechanics*. Springer Science & Business Media, 2008.
DOI: [10.1007/978-0-387-30877-7](https://doi.org/10.1007/978-0-387-30877-7)
- [50] G. M. Carlomagno and P. G. Berardi, Unsteady thermotopography in non-destructive testing, *Proc. 3rd Biannual Exchange, St. Louis/USA*, 1976, vol. 24, p. 26.
- [51] J. M. Dulieu-Barton, P. Stanley, Development and applications of thermoelastic stress analysis, *J. Strain Anal. Eng. Des.*, vol. 33, no. 2, pp. 93–104, 1998.
- [52] N. Harwood, W. M. Cummings, Calibration of the thermoelastic stress analysis technique under sinusoidal and random loading conditions, *Strain*, vol. 25, no. 3, pp. 101–108, 1989.
DOI: [10.1111/j.1475-1305.1989.tb00701.x](https://doi.org/10.1111/j.1475-1305.1989.tb00701.x)
- [53] L. Capponi, *Thermoelasticity-based analysis: collection of python packages*, 2020.
DOI: [10.5281/ZENODO.4043102](https://doi.org/10.5281/ZENODO.4043102)
- [54] R. Montanini, G. Rossi, D. Alizzio, L. Capponi, R. Marsili, A. Di Giacomo, T. Tocci, Structural Characterization of Complex Lattice Parts by Means of Optical Non-Contact Measurements, in *2020 IEEE International Instrumentation and Measurement Technology Conference (I2MTC)*, 2020, pp. 1–6.
DOI: [10.1109/I2MTC43012.2020.9128771](https://doi.org/10.1109/I2MTC43012.2020.9128771)
- [55] N. Harwood, W. M. Cummings, Applications of thermoelastic stress analysis, *Strain*, vol. 22, no. 1, pp. 7–12, 1986.
DOI: [10.1111/j.1475-1305.1986.tb00014.x](https://doi.org/10.1111/j.1475-1305.1986.tb00014.x)
- [56] S. Suzuki, Topological structural analysis of digitized binary images by border following, *Comput. vision, Graph. image Process.*, vol. 30, no. 1, pp. 32–46, 1985.
DOI: [10.1016/0734-189X\(85\)90016-7](https://doi.org/10.1016/0734-189X(85)90016-7)
- [57] D. H. Douglas and T. K. Peucker, Algorithms for the reduction of the number of points required to represent a digitized line or its caricature, *Cartogr. Int. J. Geogr. Inf. geovisualization*, vol. 10, no. 2, pp. 112–122, 1973.
DOI: [10.1002/9780470669488.ch2](https://doi.org/10.1002/9780470669488.ch2)
- [58] N. Otsu, A threshold selection method from gray-level histograms, *IEEE Trans. Syst. Man. Cybern.*, vol. 9, no. 1, pp. 62–66, 1979.
DOI: [10.1109/TSMC.1979.4310076](https://doi.org/10.1109/TSMC.1979.4310076)
- [59] G. Bradski and A. Kaehler, *Learning OpenCV: Computer vision with the OpenCV library*. O'Reilly Media, Inc., 2008, ISBN: 978-0596516130
- [60] F. Yu, V. Koltun, Multi-scale context aggregation by dilated convolutions, *arXiv Prepr. arXiv1511.07122*, 2015.
- [61] K. Shin, J. Hammond, *Fundamentals of signal processing for sound and vibration engineers*. John Wiley & Sons, 2008, ISBN: 978-0470511886.
- [62] P. Mohanty and D. J. Rixen, Operational modal analysis in the presence of harmonic excitation, *J. Sound Vib.*, vol. 270, no. 1–2, pp. 93–109, 2004.
DOI: [10.1016/S0022-460X\(03\)00485-1](https://doi.org/10.1016/S0022-460X(03)00485-1)